Numerical and experimental investigations of interdigital transducer configurations for efficient droplet streaming and jetting induced by surface acoustic waves

Mehdi H. Biroun[a], Mohammad Rahmati[a,*], Mehdi Jangi[b], Baixin Chen[c], Yong Qing Fu[a,*]

[a] Faculty of Engineering and Environment, Northumbria University, Newcastle upon Tyne, NE1 8ST, UK.

[b] Department of Mechanical Engineering, University of Birmingham, Birmingham, B15 2TT, UK.

[c] Institute of Mechanical, Process & Energy Engineering, School of Engineering & Physical Sciences, Heriot-Watt University, Edinburgh, Scotland, EH14 4AS, UK.

* Corresponding Authors:

Dr Mohammad Rahmati, Email: Mohammad.Rahmati@northumbria.ac.uk

Prof. Richard YongQing Fu, Email: richard.fu@northumbria.ac.uk

Abstract

Surface acoustic wave (SAW) based technologies have recently been explored for various sensing and microfluidic applications, and numerous experimental studies and numerical modelling of SAW streaming and liquid-solid interactions have been performed. However, the large deformation of droplet interface actuated by SAWs has not been widely explored, mainly due to the complex physics of SAW-droplet interactions and interfacial phenomena. In this paper, a computational interface tracking method is developed based on the couple level set the volume of fluid (CLSVOF) approach to simulate the interactions between liquid and acoustic waves and deformation of the liquid-air surface. A dynamic contact angle boundary condition is developed and validated by experimental results to simulate the three-phase contact line dynamics. The modified CLSVOF method is then used to study the droplet jetting and internal streaming behaviours by analyzing the energy terms within the liquid medium. Furthermore, by applying the numerical model, effects of configurations and positions of two interdigital transducers (IDTs) on droplet actuation have been investigated to achieve efficient mixing, separation, and jetting. Results show that two perfectly aligned IDTs are optimal for mixing applications. In contrast, two offset IDTs are optimal for concentration and separation applications. The maximum jetting velocity and minimum jetting time are achieved by using a pair of aligned IDTs, whereas by using the two offset IDTs, effective liquid mixing and jetting are observed which can be used in bioprinting applications.

Keywords: Surface acoustic wave, Droplet jetting, acoustic streaming, CLSVOF, interdigital transducer

1. Introduction

Integration of microfluidic functions such as droplet mixing, separation, nebulization and jetting into a lab-on-a-chip (LOC) [1] diagnosis platform is critical for various applications in biochemical research, medical diagnosis, DNA sampling, 3D bioprinting, and chemical synthesis (Cai et al., 2017; Fu et al., 2017; Khodayari Bavil and Kim, 2018). However, it is a challenge to create flows inside the droplets or channels to perform the functions at such a small scale (~ mm) because of the dominance of viscosity and interfacial tension [4-8]. Some specific technologies have been developed, such as electrically tunable superhydrophobic nanostructured surfaces (Wang et al., 2009), electrowetting (Cho et al., 2003), droplet oscillation using alternating current (AC)- electrowetting on dielectrics (EWOD) actuation (Lee et al., 2009), and magnetic actuation (Chiou et al., 2013).

Recently, surface acoustic wave (SAW) technology has been used to realize all the above mentioned microfluidic functions (Fu et al., 2010). When an RF signal is applied to interdigital transducers (IDTs) located on a piezoelectric material (such as bulk substrate of 128^{o} Y-cut $LiNbO_3$, or ZnO film on a silicon substrate), as a result of vibrations formed on the surface, an acoustic wave is generated in the solid medium which propagates as a Rayleigh wave across the solid surface (Yeo and Friend, 2009). When a droplet is located

[1] **Abbreviations**
SAW: Surface acoustic wave
SSAW: Standing surface acoustic waves
CLSVOF: coupled level set volume of fluid
IDT: Interdigital transducers
LOC: lab on a chip
EWOD: Electrowetting on dielectrics
TPCL: Three-phase contact line
LBM: Lattice Boltzmann
PISO: Pressure Implicit Split Operator
VOF: volume of fluid
SIMPLE: Semi Implicit Method for Pressure Linked Equations
DCA: Dynamic contact angle
LS: Level set

in the SAW propagation path, the acoustic energy is transferred into the liquid medium due to the mismatch between the sound velocities in the solid and liquid (Schmid et al., 2012) and drives the fluid reaching the velocities high enough to cause acoustofluidic phenomena (Fu et al., 2010). Depending on the SAW amplitude and frequency, and solid surface morphology, different microfluidic functions such as mixing, centrifugation, translation, jetting, and atomization can be achieved using SAW-based microfluidic devices (Connacher et al., 2018; Fu et al., 2017; Yeo and Friend, 2014).

Accurate simulation of droplet deformation actuated by the SAWs can be used to understand the underlying physics of the phenomena, which are often difficult to observe experimentally. Deformation of droplet interface by SAWs is a complicated phenomenon due to the interaction between the acoustic wave and fluid, surface tension change at the liquid-gas interface, and the dynamics of three-phase contact line (TPCL). Thus, analytical and numerical studies of interactions between SAW and liquid droplets have commonly been focused on the droplet mixing and internal recirculation without considering droplet deformation. Probably the first analytical work on droplet actuation by SAWs was carried out by Shiokawa et al. (Shiokawa et al., 1990, 1989) who described the acoustic force applied by the SAW to the liquid medium based on the analytical studies of Nyborg (Nyborg, 1953) and Lighthill (Lighthill, 1978) on acoustic streaming. A detailed analytical model for computation of the streaming induced by SAWs was developed by Vanneste and Bühler, and it was based on the vorticity conservation (Vanneste and Bühler, 2011). However, they only considered the fluid medium as a 2D square box placed on the surface of the SAW device. An analytical model was proposed later by Tan et al. (Tan et al., 2009a) based on the separation of scales approach to predict the jetting velocity.

A high-fidelity numerical solution of full Navier-Stokes equations for a multiphase system, applied with the acoustic waves, is arduous, computationally expensive, and sometimes inaccessible (Chen et al., 2018). Therefore, most reported computational studies have investigated the droplet actuation induced by SAWs without considering the large deformation of the liquid-gas interfaces. Instead, many studies considered the system as a single-phase liquid medium agitated by the SAWs with a fixed boundary (Alghane et al., 2012; Moudjed et al., 2015; Sankaranarayanan et al., 2008; Tang and Hu, 2015) or a free capillary boundary (Köster, 2007). With this free capillary boundary, the model worked for small deformations of the liquid [22], however, not for large deformation and breakup of droplets. Alternatively, a few studies simply assumed the liquid-gas interface to be rigid (Alghane et al., 2012; Darmawan and Byun, 2015; Quintero and Simonetti, 2013; Raghavan et al., 2010), which have been applied to reveal the internal streaming patterns within the liquid medium. For example, the effect of the fluid viscosity on the acoustic streaming was investigated by Riaud et al. (Riaud et al., 2017), who showed that the acoustic streaming patterns in a semispherical sessile droplet are dependent on both sound wave propagation and hydrodynamic flow motion.

Interfacial phenomena between the solid-liquid-gas interfaces for the liquid actuated by SAWs can be categorized into three main issues for investigation: (1) the liquid-gas interface deformation and two-phase flow problems; (2) TPCL dynamics; (3) the solid-liquid interactions. Simulation of the two-phase flow of droplet deformation within the gas (normally atmospheric air) medium has been performed using interface tracking methods (Jangi et al., 2019) and mesoscopic models such as Lattice Boltzmann (LBM) (Sheikholeslam Noori et al., 2020). The dynamics of the TPCL and the interaction between solid-liquid phases have been extensively studied for the droplet motion/impact

on the solid surface (Ahmed et al., 2014; Ashish Saha and Mitra, 2009; Griebel and Klitz, 2014; Li et al., 2016; Šikalo et al., 2005). However, these techniques have not been developed and applied for the simulation of liquid actuated by acoustic waves.

In this paper, we simulate the droplet actuation by SAWs using a model based on a 3D coupled level-set volume of fluid (CLSVOF) finite volume technique with a dynamic contact angle (DCA) model to simulate the interactions between the solid and liquid phases and TPCL dynamics. After model validation using our experimental results, numerical results are used to analyze the energy budget of the droplet, which are required for SAW induced internal streaming and jetting. Different energy terms, such as kinetic energy or viscous dissipation, are not easily measured experimentally. However, these energy terms and their effects on the physics of the flow can be investigated using the 3D numerical results, which are beneficial for design and fabrication of SAW devices for different LOC applications.

As a case study, we use the numerical method and energy analysis to optimize the IDT positions of the SAW devices for microfluidic applications such as mixing, separation and jetting. Typically, internal droplet streaming and jetting are generated using SAW devices with one IDT or a pair of aligned IDTs. Many studies applied standing surfaces acoustic wave (SSAW) designs (see Figure 1), whereas only a few studies have used two IDTs with a transversal offset between their central emission axes for internal droplet streaming and jetting (Fu et al., 2017). We hypothesize that by changing the relative positions of two opposite IDTs on the SAW device, the droplet dynamics would be significantly modified as a result of alteration in internal streaming and recirculation patterns. For example, we expect by using offset IDTs (see Figure 1(b)), a swirling flow pattern would be generated within the droplet, which could increase the

mixing efficiency. Here, we define an offset parameter, b, as the ratio between the offset distance from the edges of two IDTs, d, to the IDT aperture, w (see Figure 1 for the detailed information). For different LOC applications, a distinct type of flow is desired; therefore, we aim to use our computational tool to find an optimum value of b for each microfluidic function (e.g., mixing, separation, and jetting).

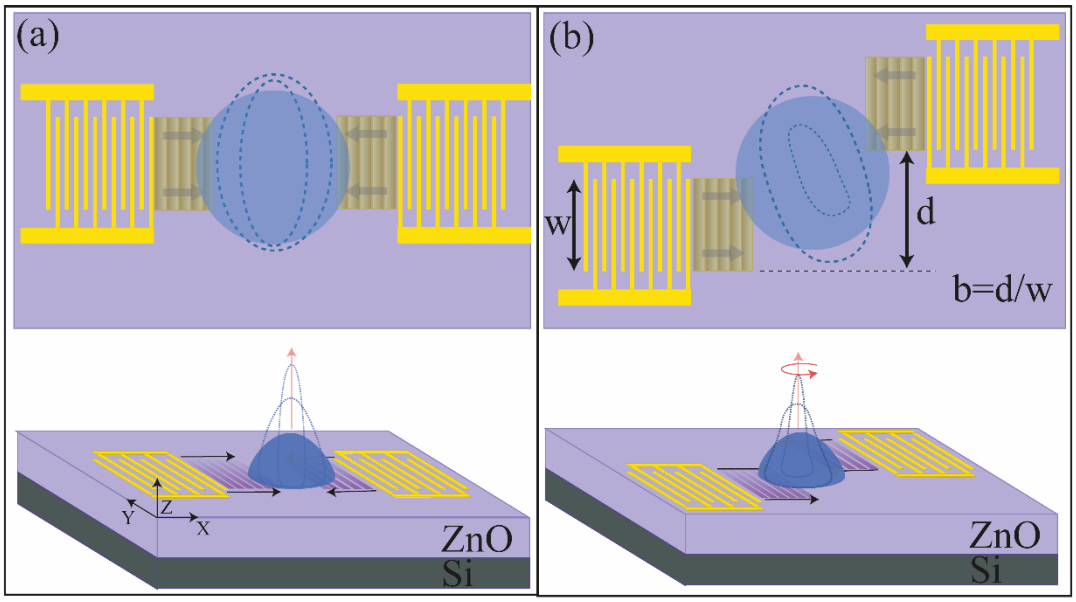

Figure 1: Schematic illustrations of droplet actuation with a ZnO/Si SAW device with (a) Aligned IDTs (b) IDTs with transversal offset. The dashed lines illustrate the expected deformation in the liquid-gas and liquid-solid interface area.

2. Mathematical modelling

2.1. CLSVOF method

The algebraic VOF solver "interFoam" of the standard OpenFOAM code (version 4.x) has been used as a basis to develop the CLSVOF code in this study (Biroun et al., 2019; Damián and Nigro, 2014). In this VOF algorithm, both liquid and gas fields are defined by the volume fraction α, which is 1 at the liquid phase and 0 at gas phase and

lies between 0 and 1 at the interface. An advection equation for the liquid volume fraction, α, is (Kalifa et al., 2020).

$$\frac{\partial \alpha}{\partial t} + \nabla.(\mathbf{U}\alpha) = 0 \quad (1)$$

where, **U** is the velocity and t is time. Temporal and spatial discretizations for interFoam calculation of this work are performed by first-order Euler method and limited van Leer TVD scheme (van Leer, 1974) respectively. Afterwards, using PIMPLE correction algorithm, the velocity field is calculated by solving the continuity and momentum. The PIMPLE algorithm is merged of a transient solver (Pressure Implicit Split Operator, PISO) and a steady-state solver (Semi Implicit Method for Pressure Linked Equations-SIMPLE) for incompressible laminar and turbulent flows. Continuity and momentum equations for an isothermal domain without phase changes is (Yu et al., 2019):

$$\nabla.U = 0 \quad (2)$$

$$\frac{\partial}{\partial t}(\rho\mathbf{U}) + \nabla.(\rho\mathbf{U}\mathbf{U}) = -\nabla p + \nabla.\boldsymbol{\tau} + \rho\mathbf{g} + \gamma_{lg}\kappa(\alpha)\nabla\alpha + \mathbf{F} \quad (3)$$

where, p is pressure, **g** is the gravitational acceleration, ρ and μ are density and dynamic viscosity respectively, $\boldsymbol{\tau} = \left[\mu\left(\frac{\partial U_j}{\partial x_i} + \frac{\partial U_i}{\partial x_j}\right)\right]$ is the viscous stress term, γ_{lg} is liquid-gas surface tension coefficient, $\kappa(\alpha)$ is the curvature of the interface, and **F** is the body force of acoustic force induced by the SAW device.

In this model, we use the approach of Shiokawa et al. (Shiokawa et al., 1989) to simulate the momentum transferred to the droplet by the SAW device. The magnitude of the body force is calculated by:

$$F = -\rho(1 + {\alpha_1}^2)^{\frac{3}{2}}A^2\omega^2 k.\exp(2[kx + \alpha_1 kz]) \quad (4)$$

where, $\alpha_1 = \sqrt{(v_S/v_L)^2 - 1}$ is attenuation factor, A is wave amplitude, ω is the angular frequency, and k is the imaginary part of the leaky SAW wave number (Sankaranarayanan et al., 2008). v_L and v_S are sound velocities in liquid and solid, respectively. x and z are the tangential and normal positions based on an origin of the coordinate at the incidence point of the SAW and droplet on the device surface, in each XZ-plane. SAW force is at its maximum at the SAW-droplet incident cell, and it attenuates exponentially in X and Z directions. The direction of the body force in each cell is calculated using the Rayleigh equation:

$$\theta_R = \sin^{-1}\frac{v_L}{v_S} \tag{5}$$

To capture a sharp interface and have a smooth transition of the physical properties along the liquid-gas interface, we merge the level set (LS) method (Sussman et al., 1996) with the explained VOF method (Sussman and Puckett, 2000) which is described in details in SI.1.

2.2. Dynamic Contact angle model

Droplet contact angle and contact angle hysteresis (i.e. the difference between advancing and receding contact angles) is a key factor in TPCL motion on solid surfaces. A resistance force is generated by contact angle hysteresis, which opposes the TPCL motion (Tao et al., 2020). It is well known that this resistance force is lower for a droplet with a higher static contact angle, θ_s, and a lower contact angle hysteresis (Aussillous and Quéré, 2001; Shen et al., 2015). To have a high-fidelity model, the effect of this force should be considered in the modelling. In this dynamic contact angle (DCA) method, instead of attempting to calculate the contact angle during the simulation at each time-step (and calculate the resistance force generated), a technique in which the contact angle

is defined as a function of TPCL velocity and contact angle hysteresis is developed. The calculated contact angle from this method is used to change the curvature of the liquid-gas interface in the TPCL region (consequently the surface tension). The developed DCA model is applied as a boundary condition to VOF and LS functions in the patches which a TPCL exists during the simulation. The details of the contact angle treatment at the TPCL cells are explained in SI.2.

To develop an accurate DCA model, a set of droplet jetting experiments are performed by a SAW device with a resonant frequency of 66.2 MHz. The experimental results of the droplet contact angle as a function of TPCL velocity are presented in Figure 2. The DCA model proposed by the Afkhami et al. (Afkhami et al., 2009) which is based on the so-called ‘‘Hoffman–Voinov–Tanner” law is used here to evaluate the DCA as a function of TPCL velocity:

$$\cos(\theta_d) = \cos(\theta_e) + C.\,Ca.\ln\left(K/\left(\frac{\Delta x}{2}\right)\right) \qquad (6)$$

where C is an empirical fitting coefficient, and k=0.2 is a constant with a dimension of length (Afkhami et al., 2009). The experimental results of droplet motion on a solid surface show that by increasing (decreasing) u_{TPCL}, the DCA tends to reach a limit at receding (advancing) contact angles. Thus, the evaluated DCA from eq. 6 is limited as:

$$\theta_d = \begin{cases} max[\theta_d, \theta_{adv}] & if \quad u_{TPCL} > 0 \\ \theta_s & if \quad u_{TPCL} = 0 \\ min[\theta_d, \theta_{rec}] & \text{if} \quad u_{TPCL} < 0 \end{cases} \qquad (7)$$

To fit the developed model to our experimental results, a comparison between the experimental results and the enhanced θ_d from eq. 6 with different values of C is

presented in Figure 2. The graph shows that there is a reasonable agreement between the experimental results and the empirical model for the selected C value of 8.45.

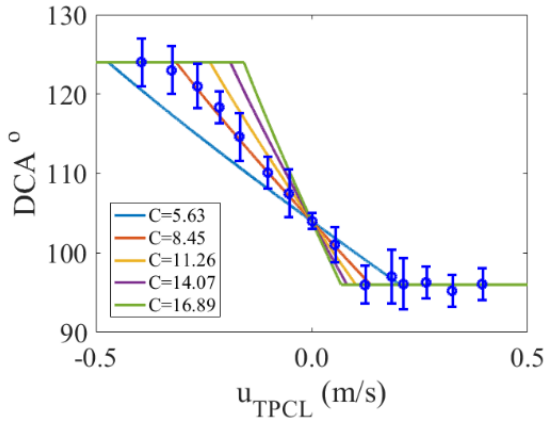

Figure 2: The variation of the DCA as a function TPCL velocity for different values of fitting coefficient, C. The blue circles are the experimental results obtained from translation experiments of the water droplet on the surface of the ZnO/Si SAW device treated with CYTOP.

The current DCA boundary condition is developed base on the existing DynamicContactAngle boundary condition in OpenFOAM. The motion of the TPCL on a no-slip boundary causes a non-integrable stress singularity which can be calculated as $\tau_{xy} = \mu \frac{u_{TPCL}}{\Delta x}$. For the calculations using fine grids, this stress could hinder the motion of the TPCL (Legendre and Maglio, 2015). It is suggested that applying Navier-slip boundary condition near the three-phase contact line area could relax the local singularity and allow the contact line motion on the solid surface (Afkhami et al., 2009). Thus, the Navier Slip boundary condition is implemented as:

$$\mathbf{u}|_{\mathbf{z=0}} - \mathbf{U_s} = \begin{cases} \xi \frac{\mathrm{d}\mathbf{u}}{\mathrm{dz}}|_{\mathrm{z=0}} & 0 < \alpha < 1 \\ 0 & \alpha = 0 \text{ or } \alpha = 1 \end{cases} \qquad (8)$$

where $\xi = \Delta x/2$ is the slip length and $\mathbf{U_s}$ is the velocity of the solid surface (Renardy and Cristini, 2001).

2.3. Computational domain and boundary conditions

The computational domain is a rectangular box for all the cases. A fully cartesian mesh is generated by blockmesh internal mesh generator of OpenFOAM. A local mesh refinement along the z-direction is extended in the entire droplet's deformation and jetting domain to increase the accuracy of the simulation in the liquid and gas-liquid interface area (see the supplementary material Figure S2). For all the cases, a droplet at room temperature (with an initial radius of 0.862 mm and a static contact angle of 104^o) is set to be stationary in the centre of the bottom plane using the setField utility of OpenFOAM. To eliminate the boundary induced disturbances, a relatively large domain is chosen for all the cases.

The developed dynamic contact angle model is applied for both ϕ and α fields on the bottom plane. The details of the input parameters, boundary conditions and solution methods are presented in supplementary materials Table S1 and S2.

3. Experimental methods

A direct current magnetron sputtering system was used to deposit a layer of piezoelectric ZnO film with a thickness of ~5 μm on the silicon (100) wafers. The deposition was carried out with a rotating substrate holder at 25 ^{o}C by sputtering a high-purity (99.99%) zinc target. During the deposition, the inlet mass flow rate of the Ar/O_2 gas mixture was kept a constant at 10/15 (in a unit of standard cubic centimetres per minute). The chamber pressure and DC plasma power were ~3.2 mTorr and 400 W. Different designed positions (see Figure 1) of interdigital transducers (IDTs) were patterned on top of the ZnO layer through photolithography and lift-off processes. The

Cr/Au electrodes with a thickness of 20/100 nm and an aperture of 5 mm were deposited using a thermal evaporator. Each IDT consists of 30 pairs of fingers with a spatial periodicity of 64 μm. As illustrated in Figure 1, different IDT position configurations for the SAW devices with the b values from 0 and 1 were fabricated for the experimental studies. An RF network analyzer (HP8752A RF network analyzer) was used to measure the resonant frequency of each SAW device. The spectra of reflection s-parameter (S_{11}) curve of the ZnO/Si SAW device is shown in Supplementary material Figure S3.

To form a hydrophobic surface, the surface of ZnO/Si SAW device was coated with 1% CYTOP solution (Asahi Glass Co.) by drop coating and a post bake for 20 min at 150 ^{o}C. The hydrophobicity of the surface was characterized by measuring the static, advancing, and retracting contact angles during volume addition and withdrawal to a sessile droplet on a droplet shape analyzer (Kruss DSA30S). The droplet static contact angle was measured to be $104^{o}\pm2^{o}$ with advancing and receding contact angles of $124^{o}\pm5^{o}$ and $96^{o}\pm3^{o,}$ respectively.

RF signals were triggered by a signal generator (Marconi Instruments 2024) and amplified with an RF amplifier (Amplifier research, 75A250) before being applied to the IDTs to excite SAWs. The power of the amplifier output signal was measured using an RF power meter (RACAL Equipment, 9104). Droplet streaming and jetting experiments were carried out at an environment temperature of 20 ± 0.5 °C and 50 ± 5% relative humidity. At this temperature, the density, kinematic viscosity, and (water-air) surface tension of DI water are 998.2 $kg.m^{-3}$, 1.004×10^{-6} $m^{2}s^{-1,}$ and 0.072 $N.m^{-1}$, respectively. Droplets of deionized (DI) water with various volumes were located at the centre of the SAW device using a micropipette. The droplet deformation was captured using a high-speed camera (HotShot 1280CC) with a macro lens (120 mm BRAND) at 2000-5000

frame per second (fps). A Matlab image processing tool was used to analyze the results. To confirm the repeatability of the experiments, each experiment was repeated three times. A schematic view of the experimental setup is illustrated in supplementary material Figure S4.

4. Results and discussion

4.1. Mesh dependency tests

Grid dependency tests were carried out by defining three cases, e.g., with coarse, normal, and fine mesh sizes. The minimum cell size for each case is presented in Table 1. The simulation time is based on parallel simulation on 4 Dual Intel Xeon E5-2680 v4 14 core 2.4 GHz CPUs (224 cores). As shown in Table 1, the average tip velocity (i.e., the time average of the vertical motion of the droplet tip during 12 ms of the jetting) is 2% higher for the Coarse case compared to those of the Fine and Normal cases.

Table 1: Test cases for grid dependency analysis.

Case	ΔX (mm)	Number of cells	Simulation time (min)	Average tip velocity (m/s)
Coarse	3.125×10^{-5}	1179648	~120	0.1447
Normal	2.50×10^{-5}	2304000	~390	0.1419
Fine	1.92×10^{-5}	5061888	~2880	0.1420

Moreover, a comparison between the temporal evolution of the droplet tip velocity (i.e., the temporal velocity of the droplet tip in Z-direction) has been made, as shown in Figure 3(a). For both the Fine and Normal cases, the tip velocity is nearly identical. However, the difference in results of the Coarse mesh case illustrates that mesh independency is not obtained with this mesh size. Overall, given the fact that simulations

with fine mesh size are computationally expensive, all the numerical cases presented in this paper are carried out with a mesh size of 2.50×10^{-5} mm.

4.2. Model validation

Experimental and simulation results are quantitatively and qualitatively compared to validate the numerical model. A 2 µl Droplet is excited by a pair of aligned IDTs (e.g., forming a conventional SSAW) with applied SAW power and frequency of 12 W and 66.2 MHz, respectively. The applied SAW power is converted to SAW amplitude by the equation of $\frac{A}{\lambda} = 6.72 \times 10^{-6}(P_D)^{1.94} + 1.52 \times 10^{-6}(P_D)^{0.91}$ to perform the simulation (Biroun et al., 2020). In this equation P_D is the applied SAW power to the IDTs in Watts and λ is the SAW wavelength in meters. Hence, the amplitude of the applied SAWs to the droplet is set to be 542 Å in numerical modelling. The computational domain is a rectangular box with a dimension of $5\times5\times6$ mm^3. The temporal evolution of the droplet contact width in the X-direction, β_x, is compared with the experimental results shown in Figure 3(b). Moreover, the computational and experimental data of droplet tip velocities during the jetting are compared, as shown in Figure 3(c). Good agreements between the experimental and simulation results are obtained for these cases. Therefore, the numerical results can be used to analyze the droplet actuation by SAWs.

Figure 4(a) shows the experimental snapshots of the droplet jetting induced by SSAWs using two aligned IDTs. The applied SAW energy from both sides generates a flow along the Rayleigh angle. As a result of the generated flow, a liquid beam is formed. Meanwhile, the solid-liquid contact area is diminished until the separation of the droplet from the surface (Jangi et al., 2019; Tan et al., 2009b). The time history of the snapshots of the XZ and YZ middle planes of the droplet overlaid by velocity vectors is shown in

Figures 4(b) and 4(c), which are obtained from the simulation results. A quantitative comparison between Figures 4(a) and 4(b) shows an acceptable agreement between the numerical and experimental results.

The comparison between the intensities of the velocity vectors in the XZ and YZ midplanes shows that the flow patterns are stronger in the YZ midplane compared to the XZ midplane (see Figures 4(b) and 4(c)). Another interesting observation in the simulation results is the difference between the velocity vectors in these two planes. The velocity vectors are rather vertical in the YZ plane, whereas in the XZ plane, some vorticities are observed to form.

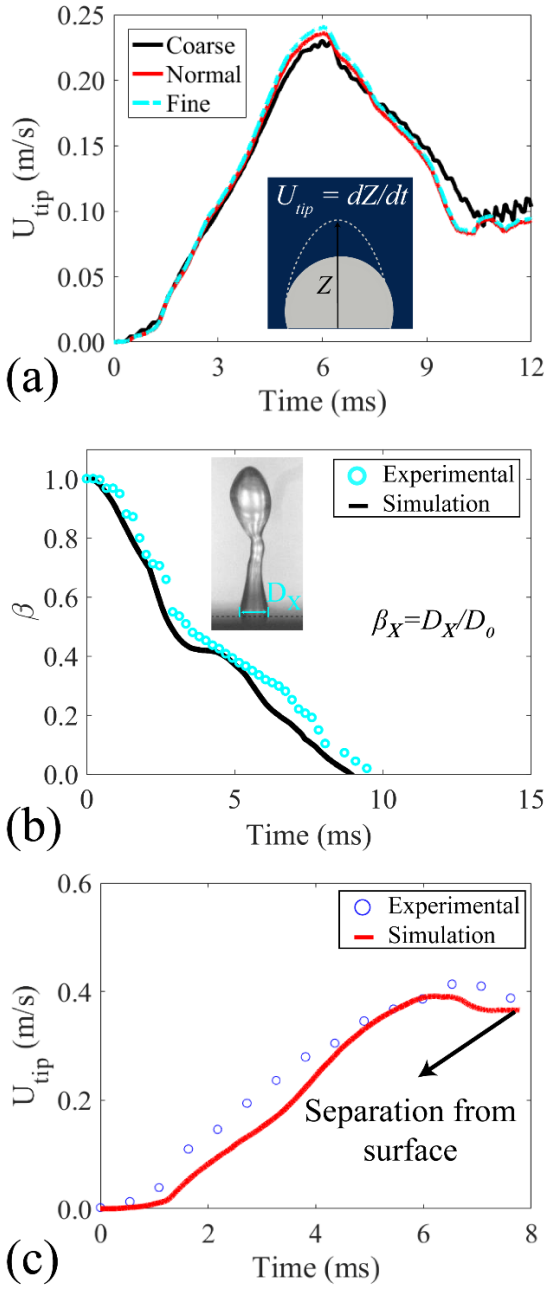

Figure 3: (a) Temporal evolution of droplet tip velocity during the jetting phenomena for different grids. (b) temporal evolution of droplet contact width in X-direction for a droplet induced by standing SAW with straight IDTs. The black line represents numerical results, and the cyan circles are obtained from experimental results. (c) A comparison between the tip velocity of the droplet for numerical and experimental results. For both cases, the droplet volume is 2µl.

Based on the simulation results, by applying the SAWs, droplet contact width starts to decrease until the jetting is complete, and the droplet is separated from the surface after 7.5 ms. Due to the liquid's inertia, at the start of the jetting and during the first 1 ms, the jet velocity is not significantly raised. During the next 5 ms, since the contact area between the liquid and solid is high, the SAW energy is quickly dissipated into the liquid medium. The transferred energy can overcome the gravitational energy, and as a result, the jet velocity is increased significantly. As the time evolves, due to the decreased solid-liquid interaction area along with jetting, the transferred SAW energy is diminished, and the droplet tip velocity is reduced, as shown in Figure 3(c).

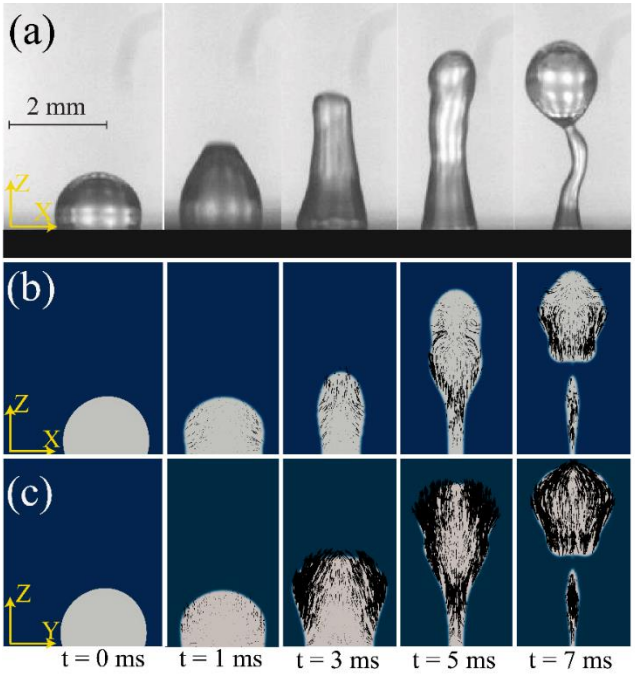

Figure 4: Experimental results of the temporal evolution of droplet jetting phenomena induced by SAWs. CFD snapshots of droplet interface overlaid by velocity vectors during the jetting process. (b) XZ middle plane, (c) YZ midplane. For both experimental and numerical results droplet volume is 2 µl. The applied SAW power to the IDTs in the experiments is 12 W. Amplitude of the applied SAW to the droplet is 360 Å.

4.3. Energy analysis of droplet vertical jetting by Standing SAW

To have a better insight of the droplet jetting phenomena and further investigate the droplet vertical jetting induced by SAWs, we focus on the energy evolution during the jetting period. During the jetting, the applied SAW energy, E_{SAW}, continuously changes the energy budget of the liquid medium. Here we define the cumulative applied SAW energy to the droplet at the given time, t_i, after the onset of SAW propagation, t_0, as:

$$E_{SAW} = \int_{t_0}^{t_i} \int (\mathbf{F}.\mathbf{U}) dV dt \tag{9}$$

The applied SAW energy causes an increase in the kinetic energy K, surface energy, E_S, and gravitational energy, P, during the jetting process. However, part of this energy is dissipated due to liquid viscosity. Here we can calculate the differences of these energies from their initial value at the stationary state. It is assumed that the kinetic energy of the droplet before applying SAW is zero (i.e., we assume there is no movement or no internal recirculation within the liquid medium for the sessile droplet). The kinetic energy of the liquid can be defined as the volume integral of the kinetic energy of the infinitesimal volume element, V, within the liquid medium, e.g.,

$$K = \int \frac{1}{2} \rho_l u^2 dV \tag{10}$$

where u is the magnitude of the liquid velocity. The surface energy S is given by (Biroun et al., 2020)

$$S = \gamma_{LV}(S_a - S_{a0}) + (\gamma_{SL} - \gamma_{SV})(S_s - S_{S0}) \tag{11}$$

where S_a and S_s are the areas of the droplet in contact with gas and solid medium, respectively. S_{a0} and S_{s0} are the initial contact areas of the droplet with the surrounding air and underneath the solid surface, respectively. γ_{SV} and γ_{SL} are the surface tension coefficients of the solid surface and solid-liquid interface. Gravitational energy is calculated from

$$P = \int \rho_l g z dV - \int \rho_l g z_0 dV \tag{12}$$

where z and z_0 are the distances of each element in the Z-direction from the solid surface at a time of t_i and a stationary state, respectively. Due to the liquid viscosity, a part of the applied energy is continuously dissipated. The viscous dissipation function, ψ, is defined as:

$$\psi = \frac{\mu}{2}\left(S_{ij}.S_{ij}\right) \tag{13}$$

Here, $S_{ij} = \left(\frac{\partial u_j}{\partial x_i} + \frac{\partial u_i}{\partial x_j}\right)$ is the strain tensor. The cumulative viscous dissipation at the given time, t_i can be calculated by:

$$E_{dis} = \int_0^{t_i} \int \psi \, dV \, dt \tag{14}$$

The results of the various energies for the simulated cases are presented in Figure 5. All the energies are normalized by the initial and total SAW energy applied to the droplet during the jetting process (7.58×10^{-7} J, which is calculated by Eq.9). It is apparent from Figure 5 that the viscous dissipation energy is two orders of magnitude lower than the other energies. Therefore, its effect on the jetting phenomena is insignificant and thus could be neglected in jetting. As time evolves during the jetting, the solid-liquid contact

area is diminished. Therefore, the transferred SAW energy, $E_{SAW,}$ from the SAW device to the droplet is decreased. Consequently, during the first 4 ms of the jetting, E_{SAW} is increased sharply. After this period, as a result of rapidly reduced solid-liquid contact area, the rate of applied SAW energy is significantly reduced.

By applying SAW energy, and during the first 4 ms of the jetting, the kinetic and surface energies of the droplet are increased as a result of the generation of an internal streaming field (See Figure 5). Within this period, the surface and kinetic energies are continuously increased. However, after 4 ms, the surface and kinetic energies do not show significant changes, and the gravitational energy of the droplet is increased. Interestingly, the kinetic and surface energies of the droplet have similar values at its separation moment. In brief, the energy analysis indicates that a part of SAW energy is converted into kinetic energy which drives the droplet upward and another part of it is used to deform the droplet interface. The energy dissipation due to liquid viscosity is negligible during the jetting process.

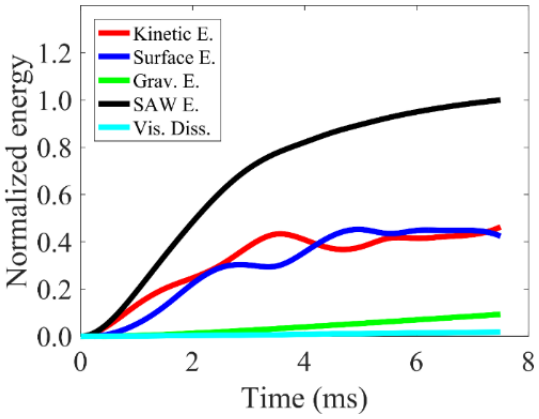

Figure 5: Temporal evolutions of the different energies obtained from CFD results. All the energies are normalized by the total amount of the SAW applied to the droplet during the jetting.

4.4. Optimization of IDT positions for microfluidic applications

Using different energy terms as the design variables for specific microfluidic applications, we investigate different IDT configurations with numerical simulations. We first focus on the internal droplet streaming without significant interface deformation in the liquid-gas interface. In general, for mixing applications, by increasing the viscous dissipation, the time to achieve an efficient and fast mixing is reduced (Sreenivasan, 2019). Therefore, for SAW-based micromixer design, it is ideal to have the maximum viscous dissipation within the liquid medium. On the other hand, for the centrifugation applications such as microseparators, the optimum design of the device should achieve the maximum internally circular streaming velocity. Therefore, the design criteria is to maximize the kinetic energy of the whole droplet.

We first compare the internal streaming patterns for two SAW device configurations: 1) SAW device with aligned IDTs (a standard SSAW); and 2) SAW device with offset IDTs (See Figures 6(a) and 6(b) for illustrations). Figure 6(a) shows the 3D internal

streaming pattern within the liquid medium induced by SAWs from two perfectly aligned IDTs. As shown in the XZ-view, The liquid is excited and pushed upward in the area close to the TPCL and then forms a strong downward flow in the Z-direction at the centre of the droplet. The YZ-view illustrates the circular patterns which are created within the liquid medium. Four zones can be distinguished in the flow patterns at the XY-plane at the bottom of the droplet. The downward flow at the centre forms a circular flow pattern. The outward flow (red arrows) are redirected along the Rayleigh angle at the TPCL by the SAW force and surface tension. Thus four vortexes are created within the liquid, which is in a good agreement with the literature (Alghane et al., 2011; Riaud et al., 2017; Sadhal, 2012). The generation of the vortices increases the rate of the viscous dissipation within the liquid.

Whereas for the SAW device with offset IDTs (as shown in Figure 6(b)), the flow pattern within the liquid is changed to one circular flow around the Z-axis in the centre of the droplet. As shown in the first and second rows of Figure 6 (b), a swirl-like circular flow is generated within the liquid (Ding et al., 2013; Fu et al., 2017). Therefore it is expected to have a lower viscous dissipation within the liquid due to the generation of lower local vorticities.

Another interesting observation is the shape change of the droplet interface after applying the SAWs. For the aligned IDTs, the droplet tip is raised as a result of the upward flow patterns (red arrows in Figure 6 (a)). Moreover, the initial circular solid-liquid interface is changed to an elliptical shape since the diameter of the solid-liquid interface is reduced in the X-direction by SAW and as a result, expanded in the Y-direction. For the IDTs with the offset design, the rotational flow changes the initial solid-liquid interface into a semi-rectangular shape with rounded edges. This is due to the deformation

and motion of the TPCL in the areas affected by SAW. This has not been observed and reported in the previously published papers because it was difficult to observe experimentally (Connacher et al., 2018; Fu et al., 2017). Meanwhile, the height of the droplet tip is lower than the aligned IDT cases since the droplet is spread on the planar surface. The same dynamics are observed in the experiments and are presented in supplementary material figure S5.

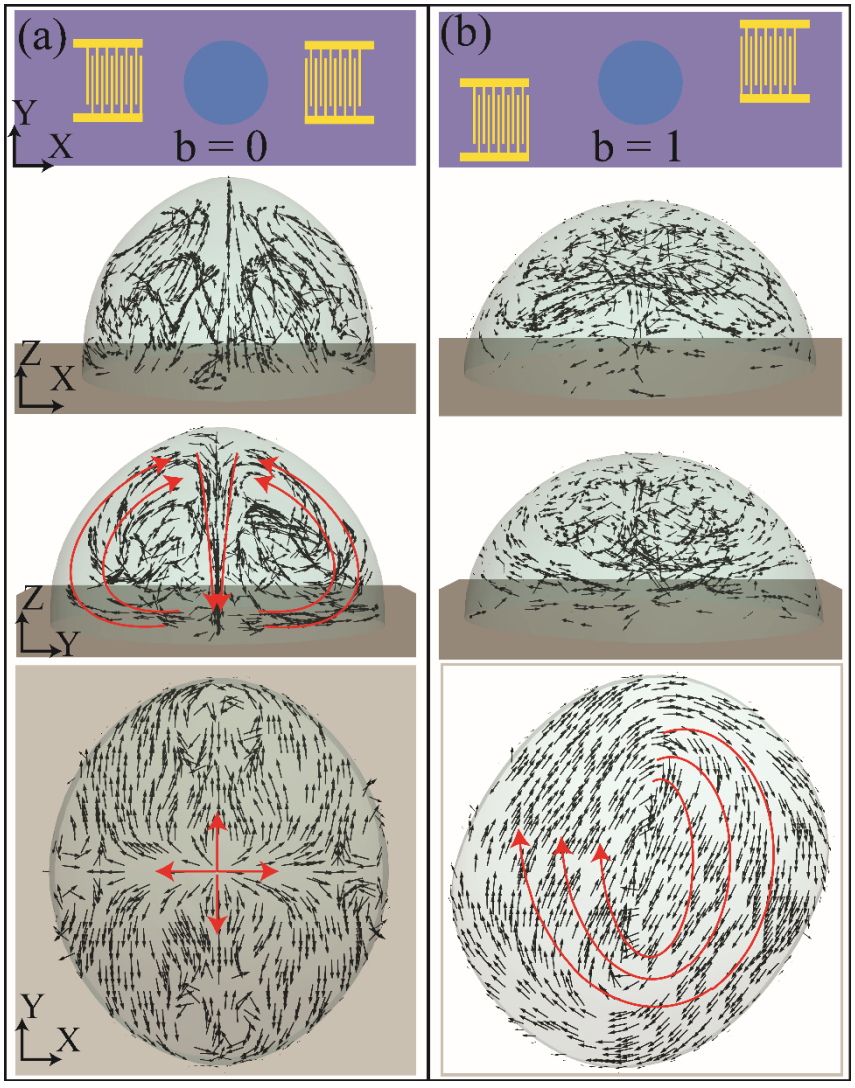

Figure 6: Internal streaming patterns for a droplet excited by a pair of (a) aligned IDTs, (b) offset IDTs. For both cases, a droplet with a volume of 2 µl is in place in the centre of the SAW device with a static contact angle of 104°. Wave amplitude and frequency for both

cases are 180 Å and 66.2 MHz, respectively. To illustrate a fully developed flow, internal streaming flow (red coloured lines) is presented after 42 ms of simulation. XZ and YZ views are shown in 3D, and the XY view is the 2D view of the bottom plane.

Figures 7 (a-b) compare the kinetic energy and viscous dissipation rate in the middle of XZ and YZ planes after 42 ms of simulation. The colour map indicates the kinetic energy per volume (right side) and viscous dissipation rate per volume (left side) enhanced by simulation results. The blue line illustrates the liquid-air interface. The coloured maps allow us to follow the changes in dissipation rates of kinetic and viscous energies. Due to the negligible motion in liquid-air interface, the surface and gravitational energies changed are simulated to be less than 4 and 2 per cent, respectively. Consequently, the applied SAW energy to the liquid medium is mostly converted into the kinetic energy, which in turn creates an internal streaming flow. However, a part of this energy is dissipated due to the fluid's viscosity.

For the aligned IDTs (see Fig. 6(a)), since there is a downward flow in the centre of the droplet, the kinetic energy is high in this region in both XZ and YZ planes. Also in the edge of the droplet in XZ plane (where is excited by SAW), the flow is in the Rayleigh angle direction, and the kinetic energy per volume is high in that region. Besides, the viscous dissipation rate is high in the areas close to the liquid-gas and liquid-solid interfaces (see the left side of Figures 7(a) and 7(b)).

On the other hand, for the offset IDT configuration (see Figure 7(b)), most of the kinetic energy is concentrated in the area close to the liquid-air interface, which shows that the rotational flow velocity is higher in this region. Moreover, since lower vorticities are generated in the stream, the viscous dissipation rate within the liquid medium is lower. The viscous dissipation rate is rather high in the areas close to the liquid-air interface.

However, unlike the aligned IDTs, viscous dissipation is much lower in the centre of the droplet. A comparison between the viscous dissipation rates shown in Figures 7(a-b) and (c-d) clearly illustrates that more energy is dissipated in the aligned IDT configuration.

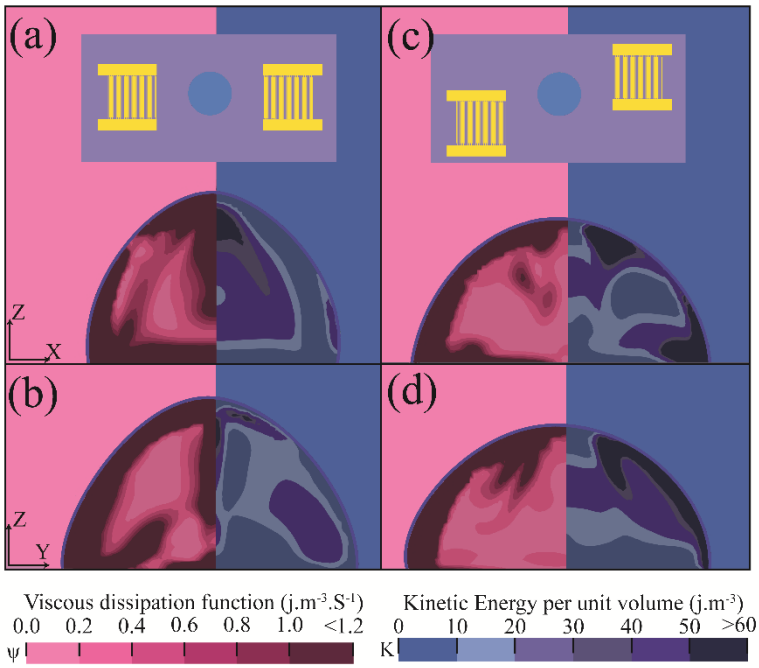

Figure 7: Kinetic energy and viscous dissipation rate fields for a droplet with internal streaming induced by a pair of aligned IDTs in (a) XZ-midplane and (b) YZ-midplane. Kinetic energy and viscous dissipation rates fields for a droplet with internal streaming induced by a pair of IDTs with offset (b=1), in (c) XZ-midplane and (d) YZ-midplane. The colour map in the left side depicts the viscous dissipation function per unit volume, and the right side shows the kinetic energy per volume. Fields are compared after 42 ms of simulation to make sure that the internal flow is steady.

These results provide an important insight into the effect of the IDT configurations in the internal streaming patterns. To use the numerical results for optimization of the IDT position design, we further investigate the gradual changes of the IDT offset value, b, on energy terms of the droplet. By progressively changing the value of b from 0 to 1.4,

we ran a series of simulations (keeping all other parameters constant) and compared the energy terms. The results are shown in Figure 8. All the energy terms are calculated after 42 ms of simulation and normalized by the aligned IDT device energy term (i.e., d=0).

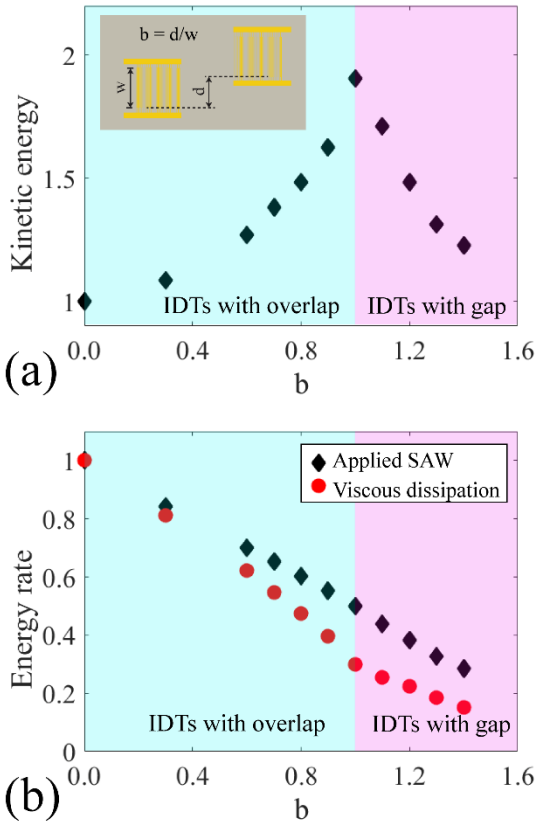

Figure 8: (a) Normalized total kinetic energy of the liquid medium after 42 ms of applying SAW as a function of IDT offset. (b) The normalized rate of applied SAW energy and viscous dissipation 42 ms after the start of SAW propagation. For all the cases, the SAW amplitude and droplet volume are kept constant at 180 Å, and 2 µl. in both graphs the values are normalized by the value of the aligned IDT case (i.e., b=0).

As shown in Figure 8(a), by increasing the value of b, the kinetic energy is increased until it reaches a peak at b=1 (i.e., the IDTs are offset). The kinetic energy of the droplet

for the offset IDTs case is ~1.9 times larger than the aligned IDTs for the same applied power to the SAW device. Meanwhile, for the IDTs with overlapping between them (i.e., b>1), the kinetic energy of the droplet is decreased. The kinetic energy of the fully developed flow is linked with the streaming velocity inside the liquid. For concentration or centrifugal applications, it is ideal for generating the maximum mixing velocity (i.e., maximum kinetic energy) by using the same applied SAW power (Alghane et al., 2011). Therefore, a SAW device with offset IDTs with b value of one is optimal for microscale mixing and separation applications.

As shown in Figure 8(b), with a successive increase in the value of b, a reduction in viscous dissipation (and thus diffusive mixing) is obtained. The reason for the decrease of viscous dissipation within the liquid could be the reduction in the local vortices by the generation of the swirl-like circular flow within the droplet. As expected, in SAW device with an IDT offset, the amount of SAW energy transferred to the liquid medium is decreased by increasing the value of b, since the solid-liquid interface induced by SAW is reduced. Thus, for mixing applications, usage of two aligned IDTs is optimal to obtain a fast and homogeneous mixing effect. The results in Figure 8 show that the optimization of an IDT configuration for various application of the SAW device can be checked by performing these simulations before physically fabricating the SAW devices with different IDT configurations.

Examples of experimentally obtained images of droplet jetting with a pair of IDTs with the offset design (see Fig. 1(b)) are presented in Figure 9. As shown by the red lines, SAW generates a swirl-like flow within the liquid droplet which deforms the interface of the droplet and triggers the liquid jetting. To explore the effect of the IDTs design on jetting by the developed numerical method, we compare the simulation results of the

jetting process of two different cases, e.g., with aligned and offset IDTs. The amplitudes of the applied SAWs and droplet volumes in all simulations are kept constants at 542 Å and 2 µl, respectively. Figure 10 illustrates the internal streaming patterns of the droplet during the jetting. For the aligned IDTs (see Figure 10(a)), after applying the SAWs, the liquid-solid interface forms a deformed oval shape from the top view as discussed above. During the jetting, this oval area is diminished until the droplet is separated from the surface. The top view of the velocity vectors illustrates that an upward flow is created inside the droplet, and this flow pushes the droplet in the vertical direction. The velocity vectors in the ZY-plane (i.e., $\mathbf{U}_{yz} = \mathbf{U}_Y.\mathbf{j}+\mathbf{U}_Z.\mathbf{k}$) shows that the area close to the liquid-gas interface has a stronger upward flow pattern compared to the centre of the droplet, which pushes the droplet jetting upwards.

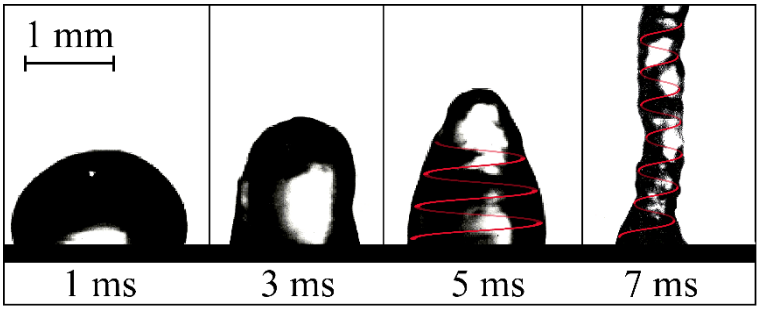

Figure 9: snapshots of 2 µl droplet jetting induced by a pair of IDTs with offset (b=1). The applied RF power to the IDTs is 9 W and the SAW device frequency is 66.54 MHz

The flow patterns for the offset IDT SAW device is presented in Figure 10(b). Similar to the internal streaming case, after SAW agitation, the solid-liquid interface is changed from its circular shape to a rectangular-like one with curved edges. During the jetting process, due to the IDTs offset, the liquid flow profile is a combination of vertical jetting and swirling flow in XY-plane. The swirling velocity field (see the XY-plane in figure 10(b)) illustrates that synchronous twisting and jetting can be obtained. This SAW

platform with the special IDT configuration can be used in bioprinting applications to mix and jet the flow toward a certain target, simultaneously.

The kinetic energy and viscous dissipation rate for the liquid jet, 4 ms after the inset of SAW propagation in XZ and YZ mid-planes, are summarised in Figure 11. As shown in Figure 11(a), for the aligned IDTs, the kinetic energy is higher at the areas closer to the liquid-air interface compared to the centre of the droplet in both XZ and YZ mid planes. This shows that the applied SAW energy creates an upward momentum which has a higher value around the liquid-gas interface region, at which the flow is pushed upward along the Rayleigh angle. Moreover, due to the larger velocity gradients at this area, more energy is dissipated by viscosity. Both kinetic energy and viscous dissipation energy are lower around the Z-axis in the centre of the droplet.

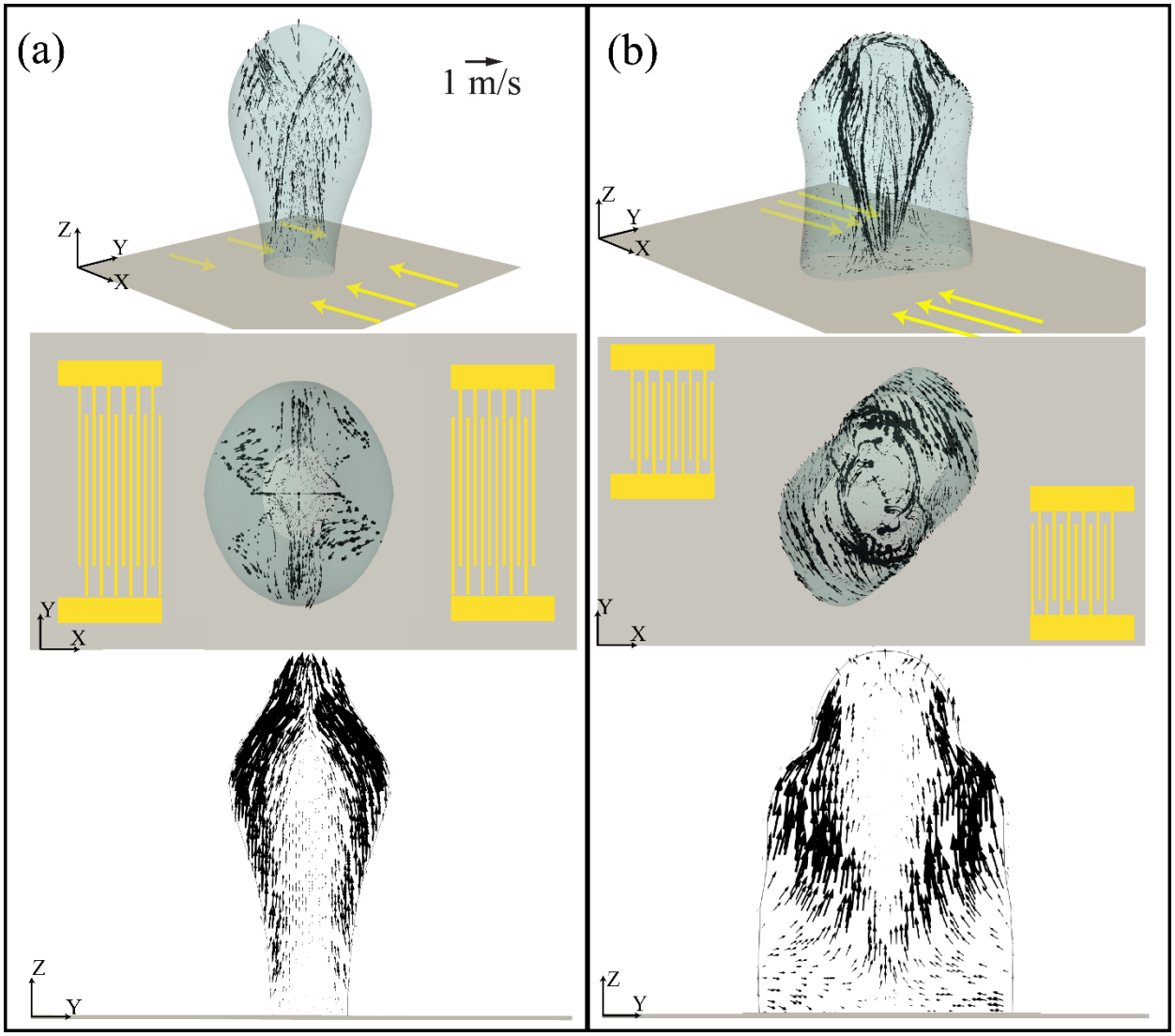

Figure 10: internal flow patterns during the jetting for a droplet excited by a pair of (a) aligned IDTs, (b) offset IDTs. For both cases, a droplet with a volume of 2 µl is in place in the centre of the SAW device with a static contact angle of 104°. Wave amplitude and frequency for both cases are 542 Å and 66.2 MHz, respectively. Internal streaming flow is compared after 4 ms of simulation. XZ and YZ views are shown in 3D, and the YZ view is the 2D view of the middle plane.

On the other hand, due to the swirling flow pattern during the jetting induced by the offset IDTs, the kinetic energy and viscous dissipation for these cases are rather different. Unlike the internal streaming cases in Figure 7, the viscous dissipation is higher for the

offset IDTs since the combined vertical jetting and twisting flows generate vorticities which in turn promotes the viscous dissipation. Also for the offset IDT case, the region close to the droplet tip does not have the maximum kinetic energy.

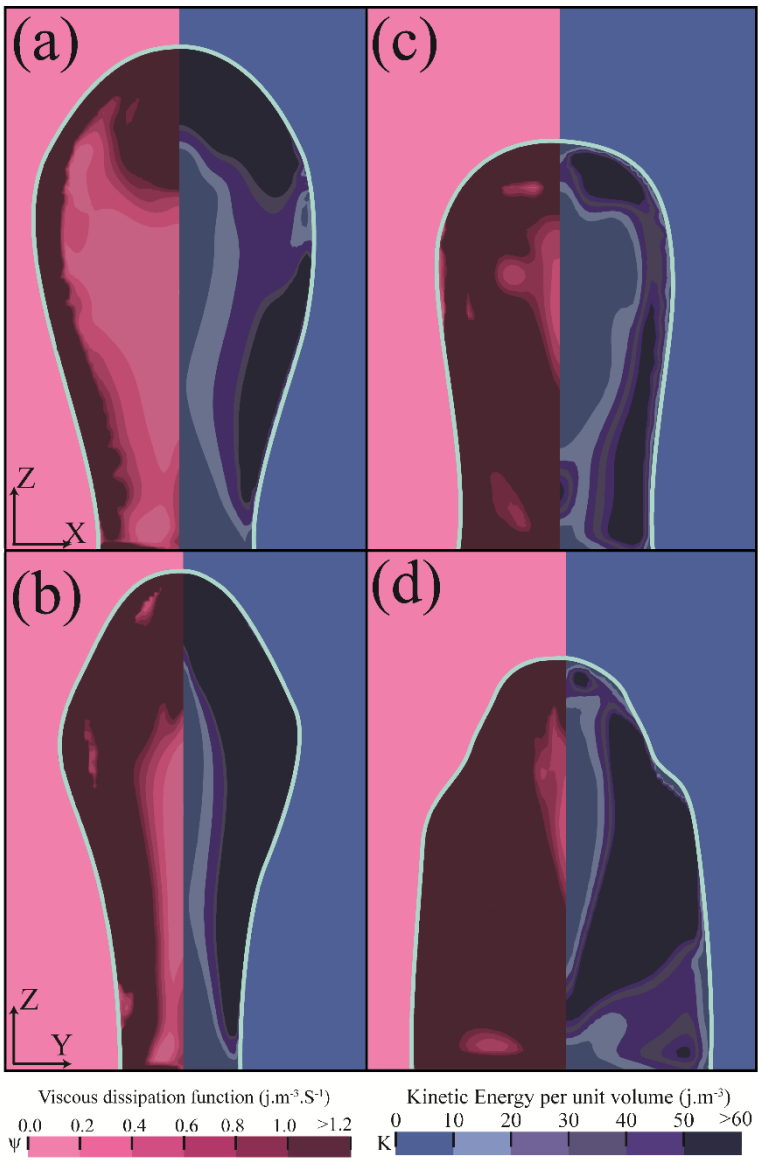

Figure 11: Kinetic energy and viscous dissipation rate fields for a droplet jetting triggered by a pair of aligned IDTs in (a) XZ-midplane and (b) YZ-midplane. Kinetic energy and viscous dissipation rates fields for a droplet with internal streaming induced by a pair of offset IDTs (b=1), in (c) XZ-midplane and (d) YZ-midplane. The colour map in the left side depicts the

viscous dissipation function per unit volume, and the right side shows the kinetic energy per volume. For both cases, a droplet with a volume of 2 µl is in place in the centre of the SAW device with a static contact angle of 104°. Wave amplitude and frequency for both cases are 542 Å and 66.2 MHz, respectively. Fields are compared after 4 ms of simulation.

Similar to the internal streaming applications, numerical results can be used to compare the effect of the IDT design on the jetting phenomena. The jetting time (i.e., the time which takes for the whole droplet to be removed from the surface) and the jetting velocity (i.e., the velocity of the droplet tip) are used as the design parameters in this section to investigate the effect of IDT configuration on droplet jetting. Droplet tip velocity and jetting time as a function of IDT offset ratio are shown in Figure 12(a). The simulation results show that with the increase of IDT offset, the tip velocity of the jet is decreased and the jetting time is increased. Unlike the internal streaming cases, the solid-liquid interface area during droplet jetting is not a constant. Thus, the total applied SAW energy to the liquid is a function of both the solid-liquid interface area and jetting time. The jetting time is increased by increasing the value of b since the total SAW energy transferred to the liquid medium is decreased and the energy dissipation rate is increased (See Figure 12(b)). As shown in Figure 12 (b), by increasing the IDT offset from 0 to 1.4, the applied SAW energy is decreased by ~42%, and the viscous dissipation is increased by 435%. As a result, the tip velocity is reduced by ~76%.

However, the comparison between the internal streaming patterns in Figure 9 illustrates that the swirl-like flow around the Z-axis (which is generated as a result of IDT offset) also affects the vertical jetting velocity. To understand the effect of the swirling on the droplet flow the Swirl Number, SN, is defined and evaluated from the velocity components as (Al-Zurfi and Turan, 2015):

$$SN = \frac{\int \sqrt{U_X^2 + U_Y^2}\, dV}{\int \sqrt{U_Z^2}\, dV} \quad (15)$$

The simulation results can obtain the temporal evolutions of the SNs for four types of the IDT designs, which are presented in Supplementary Figure S6. Numerical results show that after a transient time, the jetting flow is fully developed. Then the SNs for all the cases remain almost a constant. The SNs as a function of IDT offsets are presented in Figure 12 (c). By increasing the value of the b, the mixing flow in XY-plane becomes more dominant compared to the jetting flow along the Z-axis. Considering the results shown in Figures 12 (a-c), one can explain the differences in the flow induced by the different SAW devices. By increasing the IDT offset, the solid-liquid interface area which is excited by SAW is decreased. Thus a much lower SAW energy is transferred to the droplet (see figure 12(b)). For the SAW device with the aligned IDTs (i.e., b=0), the maximum SAW energy is applied to the droplet during the jetting time. However, as shown in Figure 12(c), the application of energy produces a flow along the Z-axis (with a maximum jetting velocity and a minimum swirling). By increasing the IDT offset, less energy is transferred to the liquid medium during the jetting. Simultaneously the jetting velocity is decreased, and interestingly recirculation in the XY-plane is increased.

Another interesting observation based on the simulation results is the increase of viscous dissipation (and thus diffusive mixing) during the jetting. Results of Figure 6 illustrate that viscous dissipation is negligible (compared to other energies) in jetting. However, for potential applications of SAW-based jetting, which may require both synchronized jetting and mixing, it is essential to optimize the IDT design and configuration. As shown in Figure 12 (b), by an increase of b values in IDT design, the

viscous dissipation is increased within the droplet, and consequently, diffusive mixing is enhanced.

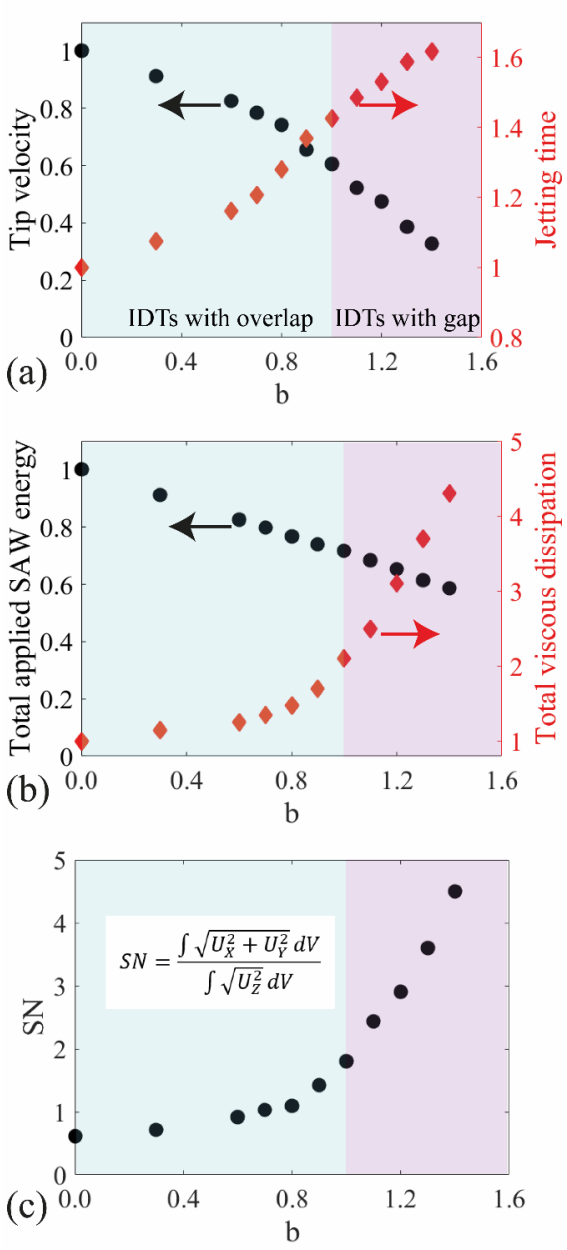

Figure 12: (a) Normalized tip velocity and jetting time as a function of IDT offset. (b) Normalized total applied SAW energy and viscous dissipation during the jetting time versus IDT offset. (c) Normalized swirl number (SN) versus IDT offset. For all the cases, SAW amplitude and droplet volume are kept constant at 542 Å and 2 µl. All the parameters are

normalized by their respective value of the aligned IDT cases. Blue area represents the IDT design with overlap between their SAW propagation path. On the contrary, the pink area represents the IDT design with a gap between the SAW propagation path.

5. Conclusions

In this paper, numerical and experimental investigations of the droplet jetting and internal streaming by SAWs was conducted. Based on the CLSVOF finite volume method, this study explored the physics of droplet jetting and internal streaming by different IDT configurations. Good agreements between the numerical and experimental results showed that the developed solver could reproduce the large deformations of a droplet induced by SAW for a reasonable computational cost. The main findings of the current study, which can be used to improve the IDT design in acoustofluidics and LOC applications, are summarised as follows:

- During the droplet jetting by SAW, both kinetic and surface energies play the main role in the jetting dynamics, whereas viscous dissipation effects can be neglected.
- For the internal droplet streaming, viscous dissipation and kinetic energy are the main energy terms affecting the internal flow and the effect of gravitational and surface energies are negligible.
- For micromixing applications of the SAW device, aligned IDT configuration is the optimal. Additionally, a pair of aligned IDTs enhance maximum jetting velocity and minimum jetting time.
- For microscale separation applications, a pair of IDTs with an offset value of one can generate the maximum internal circulation velocity.

Acknowledgements

This work was financially supported by the UK Engineering, and Physical Sciences Research Council (EPSRC) grants EP/P018998/1, and Special Interests Group of Acoustofluidics under the EPSRC-funded UK Fluidic Network (EP/N032861/1).

6. References

Afkhami, S., Zaleski, S., Bussmann, M., 2009. A mesh-dependent model for applying dynamic contact angles to VOF simulations. J. Comput. Phys. 228, 5370–5389. https://doi.org/10.1016/j.jcp.2009.04.027

Ahmed, G., Sellier, M., Jermy, M., Taylor, M., 2014. Modeling the effects of contact angle hysteresis on the sliding of droplets down inclined surfaces. Eur. J. Mech. B/Fluids 48, 218–230. https://doi.org/10.1016/j.euromechflu.2014.06.003

Al-Zurfi, N., Turan, A., 2015. A numerical simulation of the effects of swirling flow on jet penetration in a rotating channel. Flow, Turbul. Combust. 94, 415–438. https://doi.org/10.1007/s10494-014-9586-9

Alghane, M., Chen, B.X., Fu, Y.Q., Li, Y., Desmulliez, M.P.Y., Mohammed, M.I., Walton, A.J., 2012. Nonlinear hydrodynamic effects induced by Rayleigh surface acoustic wave in sessile droplets. Phys. Rev. E - Stat. Nonlinear, Soft Matter Phys. 86, 56304. https://doi.org/10.1103/PhysRevE.86.056304

Alghane, M., Fu, Y.Q., Chen, B.X., Li, Y., Desmulliez, M.P.Y., Walton, A.J., 2011. Streaming phenomena in microdroplets induced by Rayleigh surface acoustic wave. J. Appl. Phys. 109. https://doi.org/10.1063/1.3586040

Ashish Saha, A., Mitra, S.K., 2009. Effect of dynamic contact angle in a volume of fluid

(VOF) model for a microfluidic capillary flow. J. Colloid Interface Sci. 339, 461–480. https://doi.org/10.1016/j.jcis.2009.07.071

Aussillous, P., Quéré, D., 2001. Liquid marbles. Nature 411, 924–927. https://doi.org/10.1038/35082026

Biroun, M.H., Li, J., Tao, R., Rahmati, M., McHale, G., Dong, L., Jangi, M., Torun, H., Fu, Y., 2020. Acoustic Waves for Active Reduction of Contact Time in Droplet Impact. Phys. Rev. Appl. 14, 1–18. https://doi.org/10.1103/physrevapplied.14.024029

Biroun, M.H., Rahmati, M.T., Jangi, M., Tao, R., Chen, B.X., Fu, Y.Q., 2019. Computational and experimental analysis of droplet transportation/jetting behaviours driven by thin film surface acoustic waves. Sensors Actuators, A Phys. 299, 111624. https://doi.org/10.1016/j.sna.2019.111624

Cai, G., Xue, L., Zhang, H., Lin, J., 2017. A review on micromixers. Micromachines 8. https://doi.org/10.3390/mi8090274

Chen, C., Zhang, S.P., Mao, Z., Nama, N., Gu, Y., Huang, P.H., Jing, Y., Guo, X., Costanzo, F., Huang, T.J., 2018. Three-dimensional numerical simulation and experimental investigation of boundary-driven streaming in surface acoustic wave microfluidics. Lab Chip 18, 3645–3654. https://doi.org/10.1039/c8lc00589c

Chiou, C.H., Jin Shin, D., Zhang, Y., Wang, T.H., 2013. Topography-assisted electromagnetic platform for blood-to-PCR in a droplet. Biosens. Bioelectron. 50, 91–99. https://doi.org/10.1016/j.bios.2013.06.011

Cho, S.K., Moon, H., Kim, C.J., 2003. Creating, transporting, cutting, and merging liquid droplets by electrowetting-based actuation for digital microfluidic circuits. J.

Microelectromechanical Syst. 12, 70–80. https://doi.org/10.1109/JMEMS.2002.807467

Connacher, W., Zhang, N., Huang, A., Mei, J., Zhang, S., Gopesh, T., Friend, J., 2018. Micro/nano acoustofluidics: Materials, phenomena, design, devices, and applications. Lab Chip 18, 1952–1996. https://doi.org/10.1039/c8lc00112j

Damián, S.M., Nigro, N.M., 2014. An extended mixture model for the simultaneous treatment of small-scale and large-scale interfaces. Int. J. Numer. Methods Fluids 75, 547–574. https://doi.org/10.1002/fld.3906

Darmawan, M., Byun, D., 2015. Focused surface acoustic wave induced jet formation on superhydrophobic surfaces. Microfluid. Nanofluidics 18, 1107–1114. https://doi.org/10.1007/s10404-014-1503-y

Ding, X., Li, P., Lin, S.C.S., Stratton, Z.S., Nama, N., Guo, F., Slotcavage, D., Mao, X., Shi, J., Costanzo, F., Huang, T.J., 2013. Surface acoustic wave microfluidics. Lab Chip 13, 3626–3649. https://doi.org/10.1039/c3lc50361e

Fu, Y.Q., Luo, J.K., Du, X.Y., Flewitt, A.J., Li, Y., Markx, G.H., Walton, A.J., Milne, W.I., 2010. Recent developments on ZnO films for acoustic wave based bio-sensing and microfluidic applications: a review. Sensors Actuators, B Chem. 143, 606–619. https://doi.org/10.1016/j.snb.2009.10.010

Fu, Y.Q., Luo, J.K., Nguyen, N.T., Walton, A.J., Flewitt, A.J., Zu, X.T., Li, Y., McHale, G., Matthews, A., Iborra, E., Du, H., Milne, W.I., 2017. Advances in piezoelectric thin films for acoustic biosensors, acoustofluidics and lab-on-chip applications. Prog. Mater. Sci. 89, 31–91. https://doi.org/10.1016/j.pmatsci.2017.04.006

Griebel, M., Klitz, M., 2014. Simulation of droplet impact with dynamic contact angle

boundary conditions. Singul. Phenom. Scaling Math. Model. 9783319007, 297–325. https://doi.org/10.1007/978-3-319-00786-1_13

Jangi, M., Luo, J.T., Tao, R., Reboud, J., Wilson, R., Cooper, J.M., Gibson, D., Fu, Y.Q., 2019. Concentrated vertical jetting mechanism for isotropically focused Zno/Si surface acoustic waves. Int. J. Multiph. Flow 114, 1–8. https://doi.org/10.1016/j.ijmultiphaseflow.2019.02.002

Kalifa, R. Ben, Hamza, S. Ben, Saïd, N.M., Bournot, H., 2020. Fluid flow phenomena in metals processing operations: Numerical description of the fluid flow field by an impinging gas jet on a liquid surface. Int. J. Mech. Sci. 165, 105220. https://doi.org/10.1016/j.ijmecsci.2019.105220

Khodayari Bavil, A., Kim, J., 2018. A capillary flow-driven microfluidic system for microparticle-labeled immunoassays. Analyst 143, 3335–3342. https://doi.org/10.1039/c8an00898a

Köster, D., 2007. Numerical simulation of acoustic streaming on surface acoustic wave-driven biochips. SIAM J. Sci. Comput. 29, 2352–2380. https://doi.org/10.1137/060676623

Lee, H., Yun, S., Ko, S.H., Kang, K.H., 2009. An electrohydrodynamic flow in ac electrowetting. Biomicrofluidics 3, 044113. https://doi.org/10.1063/1.3274511

Legendre, D., Maglio, M., 2015. Comparison between numerical models for the simulation of moving contact lines. Comput. Fluids 113, 2–13. https://doi.org/10.1016/j.compfluid.2014.09.018

Li, Q., Zhou, P., Yan, H.J., 2016. Pinning-Depinning Mechanism of the Contact Line during Evaporation on Chemically Patterned Surfaces: A Lattice Boltzmann Study.

Langmuir 32, 9389–9396. https://doi.org/10.1021/acs.langmuir.6b01490

Lighthill, S.J., 1978. Acoustic streaming. J. Sound Vib. 61, 391–418. https://doi.org/10.1016/0022-460X(78)90388-7

Moudjed, B., Botton, V., Henry, D., Millet, S., Garandet, J.P., Ben Hadid, H., 2015. Near-field acoustic streaming jet. Phys. Rev. E - Stat. Nonlinear, Soft Matter Phys. 91, 033011. https://doi.org/10.1103/PhysRevE.91.033011

Nyborg, W.L., 1953. Acoustic Streaming due to Attenuated Plane Waves. J. Acoust. Soc. Am. 25, 68–75. https://doi.org/10.1121/1.1907010

Quintero, R., Simonetti, F., 2013. Rayleigh wave scattering from sessile droplets. Phys. Rev. E - Stat. Nonlinear, Soft Matter Phys. 88, 1–13. https://doi.org/10.1103/PhysRevE.88.043011

Raghavan, R. V., Friend, J.R., Yeo, L.Y., 2010. Particle concentration via acoustically driven microcentrifugation: MicroPIV flow visualization and numerical modelling studies. Microfluid. Nanofluidics 8, 73–84. https://doi.org/10.1007/s10404-009-0452-3

Renardy, Y.Y., Cristini, V., 2001. Effect of inertia on drop breakup under shear. Phys. Fluids 13, 7–13. https://doi.org/10.1063/1.1331321

Riaud, A., Baudoin, M., Bou Matar, O., Thomas, J.L., Brunet, P., 2017. On the influence of viscosity and caustics on acoustic streaming in sessile droplets: An experimental and a numerical study with a cost-effective method. J. Fluid Mech. 821, 384–420. https://doi.org/10.1017/jfm.2017.178

Sadhal, S.S., 2012. Acoustofluidics 13: Analysis of acoustic streaming by perturbation methods. Lab Chip 12, 2292–2300. https://doi.org/10.1039/c2lc40202e

Sankaranarayanan, S.K.R.S., Cular, S., Bhethanabotla, V.R., Joseph, B., 2008. Flow induced by acoustic streaming on surface-acoustic-wave devices and its application in biofouling removal: A computational study and comparisons to experiment. Phys. Rev. E - Stat. Nonlinear, Soft Matter Phys. 77, 1–19. https://doi.org/10.1103/PhysRevE.77.066308

Schmid, L., Wixforth, A., Weitz, D.A., Franke, T., 2012. Novel surface acoustic wave (SAW)-driven closed PDMS flow chamber. Microfluid. Nanofluidics 12, 229–235. https://doi.org/10.1007/s10404-011-0867-5

Sheikholeslam Noori, S.M., Taeibi Rahni, M., Shams Taleghani, S.A., 2020. Numerical Analysis of Droplet Motion over a Flat Plate Due to Surface Acoustic Waves. Microgravity Sci. Technol. 32, 647–660. https://doi.org/10.1007/s12217-020-09784-1

Shen, Y., Tao, J., Tao, H., Chen, S., Pan, L., Wang, T., 2015. Relationship between Wetting Hysteresis and Contact Time of a Bouncing Droplet on Hydrophobic Surfaces. ACS Appl. Mater. Interfaces 7, 20972–20978. https://doi.org/10.1021/acsami.5b06754

Shiokawa, S., Matsui, Y., Ueda, T., 1990. Study on saw streaming and its application to fluid devices. Jpn. J. Appl. Phys. 29, 137–139. https://doi.org/10.7567/JJAPS.29S1.137

Shiokawa, S., Matsui, Y., Ueda, T., Measurement, T., Ito, S., Sugimoto, M., Device, A.W., Murochi, N., Sugimoto, M., Microfluidic, C.D., Fukaya, T., Kondoh, J., 1989. Related content Experimental Study on Liquid Streaming by SAW.

Šikalo, Š., Wilhelm, H.D., Roisman, I. V., Jakirlić, S., Tropea, C., 2005. Dynamic contact

angle of spreading droplets: Experiments and simulations. Phys. Fluids 17, 1–13. https://doi.org/10.1063/1.1928828

Sreenivasan, K.R., 2019. Turbulent mixing: A perspective. Proc. Natl. Acad. Sci. U. S. A. https://doi.org/10.1073/pnas.1800463115

Sussman, M., Almgren, A.S., Bell, J.B., Colella, P., Howell, L.H., Welcome, M., 1996. An adaptive level set approach for incompressible two-phase flows. Am. Soc. Mech. Eng. Fluids Eng. Div. FED 238, 355–360.

Sussman, M., Puckett, E.G., 2000. A Coupled Level Set and Volume-of-Fluid Method for Computing 3D and Axisymmetric Incompressible Two-Phase Flows. J. Comput. Phys. 162, 301–337. https://doi.org/10.1006/jcph.2000.6537

Tan, M.K., Friend, J.R., Yeo, L.Y., 2009a. Interfacial Jetting Phenomena Induced by Focused Surface Vibrations, Physical Review Letters. https://doi.org/10.1103/PhysRevLett.103.024501

Tan, M.K., Friend, J.R., Yeo, L.Y., 2009b. Interfacial Jetting Phenomena Induced by Focused Surface Vibrations. Phys. Rev. Lett. 103, 024501. https://doi.org/10.1103/PhysRevLett.103.024501

Tang, Q., Hu, J., 2015. Diversity of acoustic streaming in a rectangular acoustofluidic field. Ultrasonics 58, 27–34. https://doi.org/10.1016/j.ultras.2014.11.015

Tao, R., Mchale, G., Reboud, J., Cooper, J.M., Torun, H., Luo, J.T., Luo, J., Yang, X., Zhou, J., Canyelles-Pericas, P., Wu, Q., Fu, Y., 2020. Hierarchical nanotexturing enables acoustofluidics on slippery yet sticky, flexible surfaces. Nano Lett. 20, 3263–3270. https://doi.org/10.1021/acs.nanolett.0c00005

van Leer, B., 1974. Towards the ultimate conservative difference scheme. II.

Monotonicity and conservation combined in a second-order scheme. J. Comput. Phys. 14, 361–370. https://doi.org/10.1016/0021-9991(74)90019-9

Vanneste, J., Bühler, O., 2011. Streaming by leaky surface acoustic waves. Proc. R. Soc. A Math. Phys. Eng. Sci. 467, 1779–1800. https://doi.org/10.1098/rspa.2010.0457

Wang, E.N., Bucaro, M.A., Taylor, J.A., Kolodner, P., Aizenberg, J., Krupenkin, T., 2009. Droplet mixing using electrically tunable superhydrophobic nanostructured surfaces. Microfluid. Nanofluidics 7, 137–140. https://doi.org/10.1007/s10404-008-0364-7

Yeo, L.Y., Friend, J.R., 2014. Surface acoustic wave microfluidics. Annu. Rev. Fluid Mech. 46, 379–406. https://doi.org/10.1146/annurev-fluid-010313-141418

Yeo, L.Y., Friend, J.R., 2009. Ultrafast microfluidics using surface acoustic waves. Biomicrofluidics 3. https://doi.org/10.1063/1.3056040

Yu, C.H., Wen, H.L., Gu, Z.H., An, R.D., 2019. Numerical simulation of dam-break flow impacting a stationary obstacle by a CLSVOF/IB method. Commun. Nonlinear Sci. Numer. Simul. 79, 104934. https://doi.org/10.1016/j.cnsns.2019.104934